Observation of quantum interference of optical transition pathways in Doppler-free two-photon spectroscopy and implications for precision measurements

Bubai Rahaman,[1] Sid C. Wright ,[2] and Sourav Dutta [1],[*]

[1]*Tata Institute of Fundamental Research, 1 Homi Bhabha Road, Colaba, Mumbai 400005, India*
[2]*Fritz-Haber-Institut der Max-Planck-Gesellschaft, Faradayweg 4-6, 14195 Berlin, Germany*

Doppler-free two-photon (DFTP) spectroscopy is a standard technique for precision measurement of transition frequencies of dipole-forbidden transitions. Here, we report the observation of quantum interference (QI) of optical transition pathways in DFTP spectroscopy of the cesium 6*S*-7*D* transitions chosen as a prototype system. The QI manifests itself as asymmetric line shapes of the hyperfine lines of the 7*D* states, observed through spontaneous emission following excitation by a narrow-linewidth cw laser. The interference persists despite the lines being spectrally well resolved. Ignoring the effect and fitting the spectrum to a Voigt profile causes large systematic shifts in the determination of the line centers, while accounting for QI resolves the apparent line shift and enables the precise determination of hyperfine splitting in the 7*D* states. We calculate the spectral line shape including the effect of QI and show that it agrees with the experimental observations. Our results are broadly applicable to other species and have implications for portable secondary optical clocks and precision measurements of hyperfine splittings, isotope shifts, and transition frequencies.

I. INTRODUCTION

Precise measurements of transition frequencies are required to benchmark theories such as quantum electrodynamics [1,2], determine fundamental physical constants [3,4], test their temporal variations [5], search for physics beyond the standard model [6–9], and improve the performance of atomic clocks [10]. One of the most straightforward and elegant techniques for high precision measurement of transition frequencies relies on Doppler-free two-photon (DFTP) spectroscopy [11,12]. It has been used to measure the hydrogen 1*S*-2*S* and 1*S*-3*S* transition frequencies with fractional uncertainties better than 4.2×10^{-15} [13] and 3×10^{-13} [4,14], respectively, from which the Rydberg constant and the proton charge radius were determined [4]. DFTP spectroscopy has also been used for the measurements of isotope shifts [9] and hyperfine splitting (HFS) of the *S* and *D* states of several atoms [15]. This includes our recent measurements of the HFS in the $7d\,^2D_{3/2}$ and $7d\,^2D_{5/2}$ states of cesium [16,17] which is motivated by the possibility of measuring the Cs *S*-*D* parity-nonconserving amplitudes [18,19]. DFTP spectroscopy is being increasingly used in portable vapor-cell based secondary optical frequency standards [20,21].

In the most common implementation of a DFTP spectroscopy experiment, light from a narrow-linewidth laser promotes atoms to an electronic excited state and the spontaneously emitted fluorescence is detected [see Fig. 1(a)]. These experiments include diligent characterization of systematic effects, for example, due to the ac Stark shift, collisional shift, and the residual Doppler shift [20–27]. We present another

systematic effect caused by quantum interference (QI) when energy levels are closely spaced. The line shift due to QI can be as large as 100 kHz, dominating the systematic error budget. The QI is subtle and remarkably survives in the presence of spontaneous emission. An analogous effect has been reported in one-photon transitions [28,29] and, recently, calculations [30] and observations [31–33] have shown that QI in one-photon transitions leads to systematic line shifts. For two-photon transitions, calculations have highlighted the important implications of QI in the context of hydrogen 1*S*-3*S* spectroscopy [34,35]. However, the QI in DFTP spectroscopy has not been experimentally observed in any system so far. We observe the effect and additionally demonstrate that it is present even when the lines are spectrally well-resolved.

As a prototype, we choose the cesium $6s_{1/2} - 7d_J$ transitions to perform DFTP spectroscopy (Fig. 1). The choice is natural because some unexplained inconsistencies were reported in our recent measurements of the HFS in Cs $7d_J$ states [16,17]. In the present more careful study of the same lines, we have discovered the QI systematic which is manifested as asymmetric line shapes and line shifts. The QI effect should be included in the uncertainty budget of all DFTP experiments irrespective of the species, the transition, or the platform (i.e., vapor cell, atomic beams, or cold atoms).

The QI observed here is analogous to a multislit experiment. As depicted in Fig. 1(b), an atom in an initial state $|i\rangle$ can be transferred to a final state $|f\rangle$ via multiple undetected resonant and/or off-resonant intermediate states $|p\rangle$ and $|e\rangle$ which are analogous to multiple slits. Therefore, as in a double-slit experiment, the probability amplitudes, rather than the probabilities, of the individual transition pathways must first be added and then the modulus squared to determine the probability of reaching the final state, which in the experiment
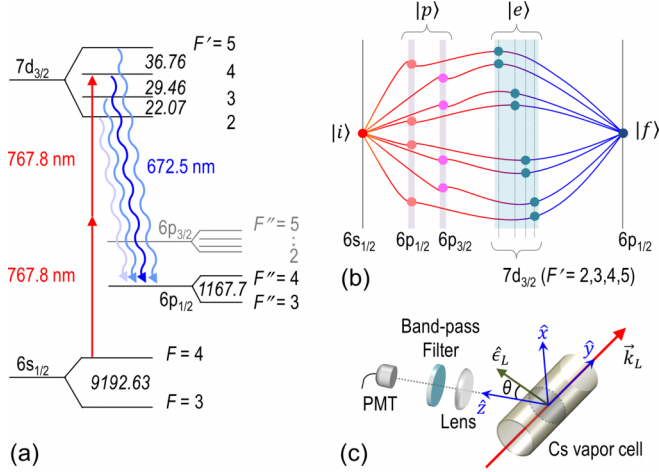
*sourav.dutta@tifr.res.in

FIG. 1. Schematic representation of the experiment. (a) Partial energy level diagram (not to scale) of ^{133}Cs. Numbers in italics are the HFS in MHz. Two-photon excitation of the $7d_{3/2}$ state is depicted with straight lines and the relevant spontaneous decay channels are depicted by wavy lines. (b) Schematic representation of interfering quantum pathways, analogous to a multislit interference experiment. (c) Sketch of the experimental setup. The laser beam with wave vector $\vec{k}_L$ propagates along the $\hat{y}$ direction, is linearly polarized along $\hat{\epsilon}_L$ in the $\hat{x}-\hat{z}$ plane, and makes an angle θ with the $\hat{z}$ axis. The laser beam is then retroreflected. The detection is along the $\hat{z}$ direction. The spectral bandwidth (10 nm) of the bandpass filter is orders of magnitude larger than the $7d_J$ HFS, and cannot be used to distinguish between the decay channels; thus obscuring the knowledge of the intermediate state $|e\rangle$ and enabling the QI to survive.

is proportional to the fluorescence intensity. One can visualize each pathway as an induced oscillating dipole that generates an electric field and the fields from several of these dipoles interfere. As a result, the relative intensity of the hyperfine lines becomes dependent on the amount of QI and the observation direction [Fig. 1(c)], and the fluorescence line shape can no longer be considered as a sum of independent Lorentzian or Voigt profiles. The formal theoretical calculations and the resulting line shapes are presented later in the article. Note that the linewidth of the laser is ∼100 times narrower than the HFS and therefore the observed QI effect cannot be attributed to laser-induced superposition of excited states or quantum beats.

II. EXPERIMENTAL RESULTS

The energy level diagram relevant to the experiment is shown in Fig. 1(a) and the sketch of the setup is shown in Fig. 1(c). The $6s_{1/2}$ ($F = 3$) and $6s_{1/2}$ ($F = 4$) states are equally populated in a Cs vapor cell but can be selectively excited to the $7d_{3/2}$ ($7d_{5/2}$) state using a narrow-linewidth cw laser near 767.8 nm (767.2 nm). The different hyperfine levels F' are excited by tuning the frequency of the excitation laser using an acousto-optic modulator (AOM) in double-pass configuration [16,17]. The spontaneous emission at 672.5 nm (695 nm) due to the $7d_{3/2} \rightarrow 6p_{1/2}$ ($7d_{5/2} \rightarrow 6p_{3/2}$) decay is recorded as the laser frequency is tuned, generating the hyperfine spectrum for the $7d_{3/2}$ ($7d_{5/2}$) state. The chosen decay channel has the highest branching ratio ∼0.65 (∼0.77)

[36] and the emitted light cannot be reabsorbed by the ground state Cs atoms resulting in a high signal-to-noise ratio (SNR) of the order 10^3. Additional details of the experiments are provided in Appendix A and the Supplemental Material (SM) [37].

We show the experimentally measured spectra for the $7d_{3/2}$ ($7d_{5/2}$) state in Fig. 2 (Fig. 3) for different angles θ between the linearly polarized incident light and the detector direction. Panels (a) and (b) depict the spectra recorded when atoms are excited from the $6s_{1/2}$ ($F = 3$) and $6s_{1/2}$ ($F = 4$) levels, respectively. Each spectrum of the $7d_{3/2}$ ($7d_{5/2}$) state is fit to a combination of four (five) independent Voigt line shapes, from which we determine the four (five) line centers of the individual peaks, four (five) Lorentzian widths, four (five) Gaussian widths, four (five) peak heights, and one (one) background offset. The fit residual is shown below each spectrum. The HFS is obtained from the difference in the line centers and is plotted in panel (c).

The residuals have different signs on the two sides of the line center for all angles other than $\theta \sim 53°$. The dispersive shaped pattern in the residuals provides striking evidence of asymmetry in the peaks. The dispersive pattern disappears at $\theta \sim 53°$ (see Fig. 2) suggesting that the Voigt profile is the correct line shape near this angle. Furthermore, it is seen that the slope of the dispersive pattern changes sign at $\theta \sim 53°$. Another striking observation [see Figs. 2(c) and 3(c)] is that the measured $7d_J$ state HFSs are different when experiments are performed by exciting atoms from the $6s_{1/2}$ ($F = 3$) and $6s_{1/2}$ ($F = 4$) levels, except when experiments are performed at $\theta \sim 53°$, i.e., near the "magic angle" $\theta_m = 54.7°$. Deviations as large as 100 kHz are seen. These observations, when compared with calculations (see Figs. 4 and 5), prove the existence of QI of optical transition pathways.

III. THEORETICAL ANALYSIS

We follow the perturbative treatment developed in Ref. [34] to theoretically calculate the spectra. The second-order dipole matrix element for the $|i\rangle \rightarrow |e\rangle$ two-photon excitation process [see Fig. 1(b)] is $Q_{ei}^{\mu\nu} = \sum_p \frac{D_{ep}^\nu D_{pi}^\mu + D_{ep}^\mu D_{pi}^\nu}{\hbar(\omega_{pi} - \omega_L)}$. Here D_{ep}^ν (D_{pi}^μ) is the dipole matrix elements between $|e\rangle$ and $|p\rangle$ ($|p\rangle$ and $|i\rangle$) with $|p\rangle$ denoting the intermediate $6p_J$ states accessible via one-photon transitions, μ and ν are the incoming and retroreflected laser polarizations (identical in our case), and ω_L is the laser frequency. The subsequent radiative decay $|e\rangle \rightarrow |f\rangle$ entails a dipole matrix element D_{fe}^η, where η is the polarization of the emitted radiation. The emitted intensity takes the form $I^{\eta\mu\nu} \propto \sum_{if} |\sum_e \frac{D_{fe}^\eta Q_{ei}^{\mu\nu} H(\omega_{ef})}{\omega_{ei} - 2\omega_L - i\Gamma_e/2}|^2$, where $H(\omega_{ef})$ is proportional to the density of states and Γ_e is the spontaneous decay rate. Since the amplitudes of the various processes are added before taking the modulus square, cross terms are obtained in addition to the standard Lorentzian terms. The cross terms introduce an additional θ dependence to the fluorescence emission pattern. This θ dependence is over and above that arising from the dipole emission pattern alone, and causes asymmetry in the line shape. In general, the cross terms depend on θ, specifically on $P_2(\cos\theta)$, but identically go to zero when $3\cos^2\theta - 1 = 0$, i.e., $\theta \equiv \theta_m = 54.7°$, in which case the line shape can be represented as a symmetric
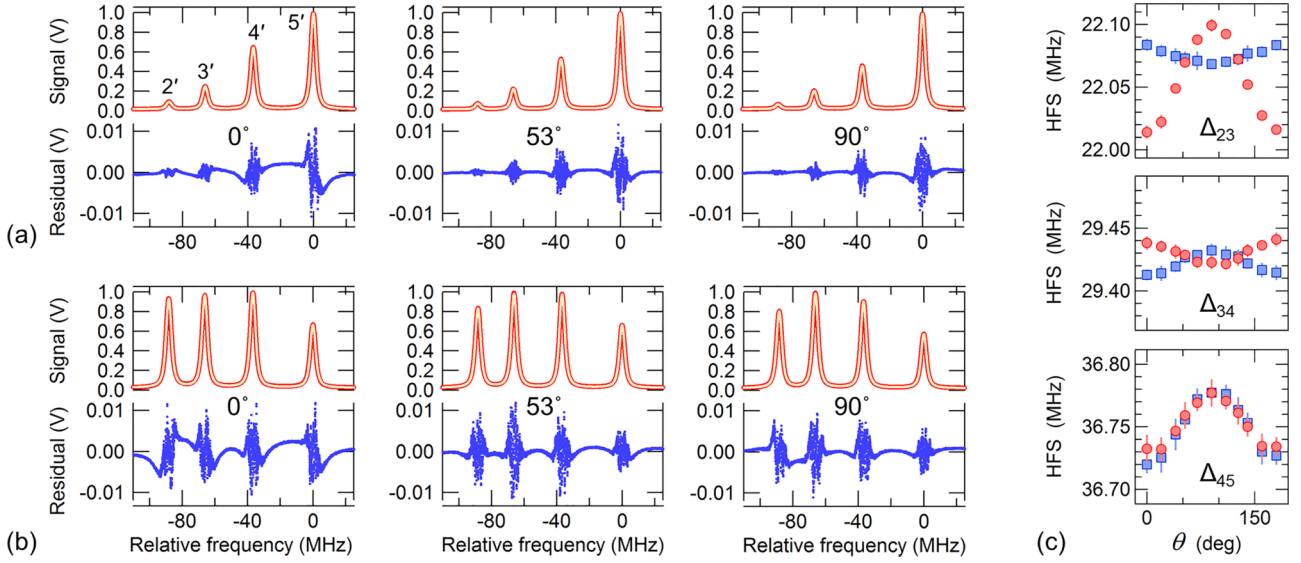
FIG. 2. Spectroscopy of the $7d_{3/2}$ state. (a),(b) Spectra for the $6s_{1/2}(F = 3) \rightarrow 7d_{3/2}(F' = 2, 3, 4, 5)$ and the $6s_{1/2}(F = 4) \rightarrow 7d_{3/2}(F' = 2, 3, 4, 5)$ transitions, respectively, at three different values of θ viz. $0° \pm 2°$, $53° \pm 2°$, and $90° \pm 2°$. Red lines are the measured data and the superimposed white lines are the fits to a combination of four independent Voigt profiles, each of which is symmetric around the line center. The residuals (blue dots) show the difference between the data points and the fitted function. For $\theta = 0°$, the asymmetry in the residuals on either side of the line center is most clearly visible in the $6s_{1/2}(F = 3) \rightarrow 7d_{3/2}(F' = 5)$ and the $6s_{1/2}(F = 4) \rightarrow 7d_{3/2}(F' = 2)$ lines. The asymmetry is reduced to the noise level of the experiment for $\theta = 53°$ and reappears for $\theta = 90°$. (c) The $7d_{3/2}$ state HFS Δ_{23}, Δ_{34}, and Δ_{45} obtained from the Voigt fits depend on θ due to QI. Blue squares: excitation from the $6s_{1/2}(F = 3)$ state, red circles: excitation from the $6s_{1/2}(F = 4)$ state. The HFS for the two cases agree when $\theta \sim 54.7°$ (and equivalently also at $\theta \sim 125.3°$) where the QI effect vanishes.

Lorentzian profile (or a symmetric Voigt profile, if transit time broadening and collisional broadening are included). In a real experiment, the solid angle Ω_c subtended by the imaging lens is nonzero, i.e., θ is spread out. For small values of Ω_c (i.e., $\Omega_c \ll 4\pi$), as in our experiment, the interference term reduces

in magnitude but is still appreciable. However, it becomes zero for $\Omega_c = 2\pi$ or 4π, i.e., in experiments where fluorescence is collected from all directions. The expressions for the full quantum interference line shape for arbitrary θ and additional details on the model are provided in Appendix B.

In Figs. 4(a), 4(b) and 5(a), 5(b), we plot the computed spectra taking into consideration the QI effect, detector geometry, solid angle, and a Gaussian broadening to mimic the transit-time and collisional broadening seen in the experiment. The HFSs are supplied as input (from the experimental measurements at $\theta \sim \theta_m$) and all other parameters are fixed at their respective theoretical values. The computed spectra reproduce the experimentally observed spectra (Figs. 2 and 3). We fit the computed spectra to Voigt line shapes in an identical manner as done for the experimental data. The fit residuals show the same features that are experimentally observed in Figs. 2 and 3. Moreover, the extracted HFS vs θ plots [Figs. 4(c) and 5(c)] closely reproduce our experimental observations [Figs. 2(c) and 3(c)], not just qualitatively but also quantitatively. The experimental data (Figs. 2 and 3) and the computed spectra (Figs. 4 and 5) together provide the necessary evidence in support of the observation of QI of optical transition pathways in DFTP spectroscopy and highlights that fitting to a Voigt line shape results in apparent line shifts.

Finally, we fit the experimental data to the QI line shape model and found that the dependence of HFS on θ is much reduced but not completely removed. The fitting parameters were the line centers, a common Lorentzian linewidth, a common Gaussian linewidth, an overall amplitude, and an overall offset. All other parameters were fixed: the relative peak heights were fixed at their theoretical values; Ω_c and θ were fixed at their measured values. That the θ dependence of the
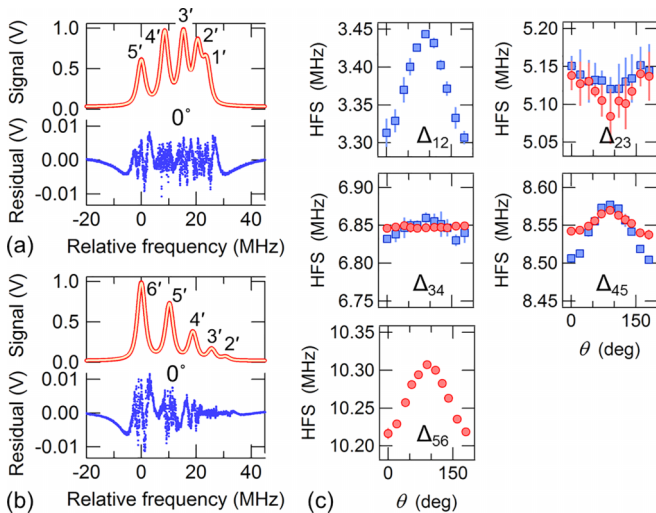

FIG. 3. Spectroscopy of the $7d_{5/2}$ state. The colour code and notations follow the conventions set in Fig. 2. (a),(b) Representative spectra at $\theta = 0°$ for the $6s_{1/2}(F = 3) \rightarrow 7d_{5/2}(F' = 1, 2, 3, 4, 5)$ and the $6s_{1/2}(F = 4) \rightarrow 7d_{5/2}(F' = 2, 3, 4, 5, 6)$ transitions. The asymmetry in the residuals is most clearly visible in the $6s_{1/2}(F = 3) \rightarrow 7d_{5/2}(F' = 5)$ and the $6s_{1/2}(F = 4) \rightarrow 7d_{5/2}(F' = 6)$ lines. (c) The $7d_{5/2}$ state HFS Δ_{12}, Δ_{23}, Δ_{34}, Δ_{45}, and Δ_{56} obtained from the Voigt fits depend on θ.
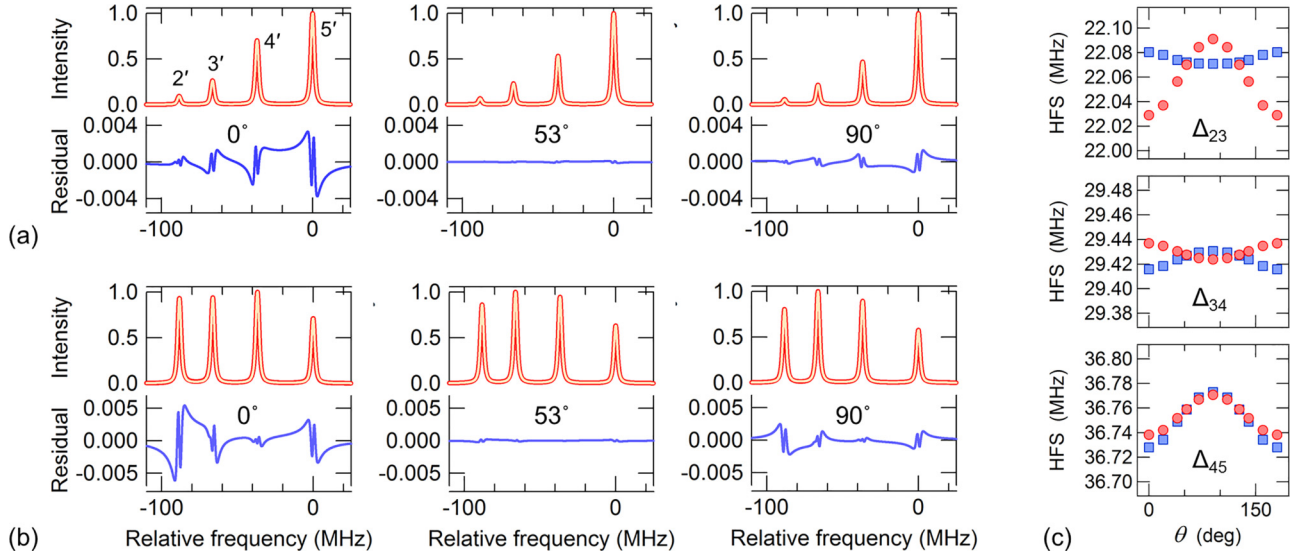
FIG. 4. Simulated spectra of $7d_{3/2}$ state. (a),(b) The $6s_{1/2}(F = 3) \rightarrow 7d_{3/2}(F' = 2-5)$ and the $6s_{1/2}(F = 4) \rightarrow 7d_{3/2}(F' = 2-5)$ transitions, respectively. The red lines are the simulated data and the superimposed white lines are the fits to a combination of four independent Voigt profiles. The residuals (blue line) are asymmetric on either side of the line center except when $\theta = 53°$, where the residuals tend to zero. The residuals change sign at $\theta \sim 54.7°$. (c) The $7d_{3/2}$ state HFSs obtained from the Voigt fits vary with θ due to QI. The HFS when exciting from the $6s_{1/2}(F = 3)$ state (blue squares) and the $6s_{1/2}(F = 4)$ state (red circles) agree at $\theta \sim 54.7°$ (and equivalently also at $\theta \sim 125.3°$) where the QI vanishes.

HFS is reduced, despite a smaller number of free parameters in the fitting function, supports the efficacy of the QI model. It is difficult to accurately define the true fluorescence volume within the laser focus (see the SM [37]), and we believe this explains the remnant θ dependence we observed.

IV. HYPERFINE COUPLING CONSTANTS

We report the recommended values of HFS in Table 1S of the SM [37] along with the statistical uncertainties. We account for the systematic uncertainties arising from the ac Stark shift ($\sim$3 kHz), collisional shift ($\sim$5 kHz), Zeeman shift ($<$1 kHz), and second order Doppler shift ($\sim$0.5 kHz),

as discussed in the SM [37]. The statistical and systematic uncertainties are added in quadrature to estimate the total uncertainty in the HFS and the hyperfine coupling constants (HCCs). We report the values of the HCCs in Table I. The expressions used to calculate the magnetic dipole (A), the electric quadrupole (B), and the magnetic octupole (C) coupling constant from the measured HFSs are provided in the SM [37]. The recently reported corrections due to the second order effects [40,41] are included in our analysis.

We improve the precision of the HCCs by at least an order of magnitude compared to experimental reports from other groups [23–27] and improve on our earlier works [16,17] by accounting for QI. Notably, using the calculated values of $C/\Omega = 0.0195(-0.0180)$ kHz$/(\mu_N \times b)$ for the $7d_{3/2}$ ($7d_{5/2}$) state [40] and our values of C, we determine $\Omega = -15 \pm 20(1 \pm 44)\mu_N \times b$. While this puts bounds on the value of the nuclear magnetic octupole moment (Ω), the error bars are still too large to constrain nuclear model calculations. This indicates that higher precision experiments must be undertaken in the future. On the other hand, the experimentally determined values of A and B are precise but not in perfect agreement with the theoretical values [38–40] suggesting that more sophisticated theoretical calculations of HCCs for the $7d$ and other nd states need to be undertaken.
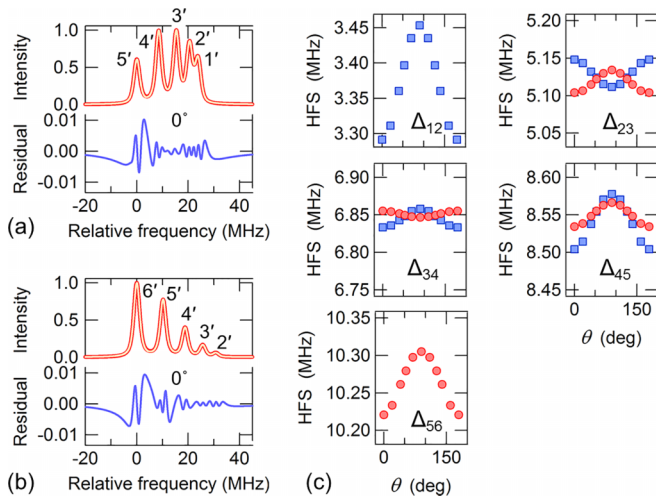

FIG. 5. Simulated spectra of $7d_{5/2}$ state. (a),(b) The $6s_{1/2}(F = 3) \rightarrow 7d_{5/2}(F' = 1-5)$ and the $6s_{1/2}(F = 4) \rightarrow 7d_{5/2}(F' = 2-6)$ transitions, respectively. (c) The $7d_{5/2}$ state HFS obtained from the Voigt fits.

V. SUMMARY

In summary, we show that the QI between optical transition pathways leads to asymmetric line shapes in DFTP spectroscopy. If unaccounted for, in the specific case of Cs $7d_J$ states, this causes apparent shifts of several tens of kHz in determination of line centers. Importantly, the interference effect is present although the lines are well resolved and the laser has narrow linewidth. Therefore its influence must be

TABLE I. The hyperfine coupling constants determined in this work and a comparison with earlier reports.

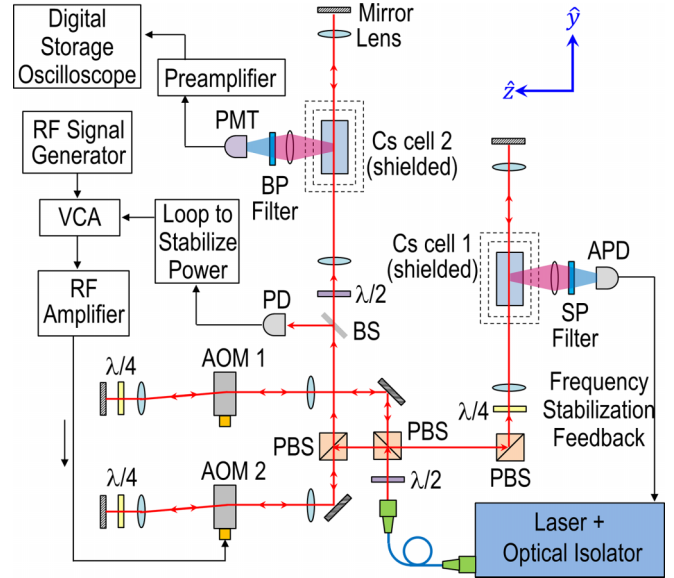|	HCC	This work	Ref. [17]	Ref. [16]	Ref. [23]	Ref. [24]	Ref. [25]	Ref. [26]	Ref. [27]	Ref. [38]	Ref. [39]	Ref. [40]
$7d_{3/2}$	A (MHz)	7.3547(8)	7.3509(9)		7.386(15)	7.38(1)	7.36(3)	7.36(7)	7.39(6)	7.48	7.88	7.42(37)
	B (MHz)	−0.017(7)	−0.041(8)		−0.18(16)	−0.18(10)	−0.1(2)	−0.88(87)	−0.19(18)			−0.0249(9)
	C (kHz)	−0.3(4)	−0.03(53)									
$7d_{5/2}$	A (MHz)	−1.7110(3)		−1.7087(6)	−1.717(15)			−1.81(5)	−1.79(5)	−1.13	−1.42	−1.26(16)
	B (MHz)	−0.027(7)		0.050(14)	−0.18(52)			1.01(1.06)	1.05(29)			−0.0339(12)
	C (kHz)	−0.02(80)		0.4(1.4)								

FIG. 6. Schematic diagram of the experimental setup. AOM: acousto-optic modulator; PMT: photomultiplier tube; PD: photo-diode; APD: avalanche PD; BS: beam sampler; PBS: polarizing beam splitter; BP: bandpass; SP: short pass; VCA: voltage controller attenuator.

considered in all other fluorescence-based DFTP spectroscopy experiments irrespective of the species, the transition, or the platform (i.e., vapor cell, atomic beam, or cold atoms) used. The effect of QI vanishes at the magic angle of 54.7° between the laser polarization and the detector axis, thus providing a convenient practical alternative to the full QI model fitting.

ACKNOWLEDGMENTS

APPENDIX A: EXPERIMENTAL SETUP

Figure 6 shows the schematic diagram of the experimental setup. The laser beam is divided into two parts. The first beam's frequency is shifted using AOM1 and sent to Cs cell 1. The frequency of the laser is stabilized using an electronic feedback from the Doppler-free two-photon spectroscopy in Cs cell 1. The second beam is sent to AOM2 and then to Cs cell 2. The hyperfine spectra (e.g., Figs. 2 and 3) are obtained by tuning the radio frequency (rf) applied to AOM2 and recording the fluorescence from Cs cell 2 on a PMT. The AOMs are carefully aligned in cat's eye double-pass configu-ration to ensure that the laser beam direction does not change when the rf is tuned.

A lens of focal length 20 cm focuses the beam to a $1/e^2$ radius $r = 63 \pm 3\,\mu\text{m}$ and Rayleigh range of 16 mm. The fluorescence collection lens system has a diameter of 25 mm and is placed ∼67 mm from the excitation region. The 10-nm bandpass (BP) filter has center wavelength 670 nm (694 nm) for the $7d_{3/2}$ ($7d_{5/2}$) experiments and cannot resolve between the different decay channels shown in Fig. 1(a). The laser
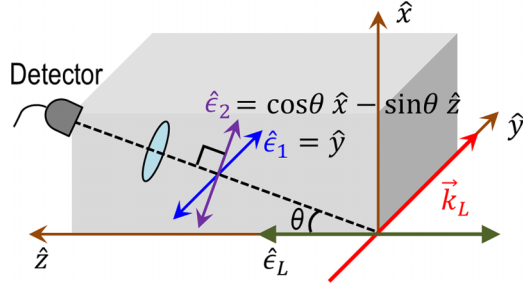
FIG. 7. Excitation and detection geometry.

power incident on Cs cell 2 is stabilized using a feedback loop that controls the rf power to AOM2. The Cs cells are heated to $\sim 135\,°C$ ($\sim 100\,°C$) for the $7d_{3/2}$ ($7d_{5/2}$) state measurements and are placed in two layers of mu-metal shielding to reduce the residual magnetic field to ~ 2 mG. The linear polarization of the laser light incident on Cs cell 2 is controlled using a half-wave plate.

APPENDIX B: DETAILS OF SIMULATED SPECTRA

The excitation and detection geometry relevant for the calculations is shown in Fig. 7. Note that, for simplicity, the axes convention is defined differently compared to the main text but the results are independent of the convention chosen.

$$\langle e|d_q|f\rangle = (-1)^{J(f)+L(e)+S+1}\sqrt{(2J(e)+1)(2J(f)+1)}\begin{Bmatrix} L(e) & J(e) & S \\ J(f) & L(f) & 1 \end{Bmatrix}(-1)^{F(f)+J(e)+I+1}\sqrt{(2F(e)+1)(2F(f)+1)}$$

$$\times \begin{Bmatrix} J(e) & F(e) & I \\ F(f) & J(f) & 1 \end{Bmatrix}(-1)^{(F(e)-M(e))}\begin{pmatrix} F(e) & 1 & F(f) \\ -M(e) & q & M(f) \end{pmatrix}\langle e||d||f\rangle. \tag{B2}$$

Here, the reduced matrix element $\langle e||d||f\rangle$ is independent of J, F and is common to all terms for a particular transition.

The two-photon matrix elements $Q(\hat{\epsilon}_L, i, e)$ are given by

$$Q(\hat{\epsilon}_L, i, e) = \sum_p \frac{\langle i|\boldsymbol{d}.\hat{\epsilon}_L|p\rangle\langle p|\boldsymbol{d}.\hat{\epsilon}_L|e\rangle}{\hbar(\omega_L - \omega_{pi})}, \tag{B3}$$

where the sum runs over all intermediate states $|p\rangle$. In practice, it is sufficient to consider only the intermediate $6p_{1/2}$ and $6p_{3/2}$ states since the detuning $\omega_L - \omega_{pi}$, which appears in the denominator, is much larger for other states and thus their contribution to the sum is small. For the $6s_{1/2} \to 7d_{5/2}$ two-photon transition, the only intermediate state that needs to be considered is the $6p_{3/2}$ state transition. For the $6s_{1/2} \to 7d_{3/2}$ two-photon transition, we must include both the $6p_{1/2}$ and $6p_{3/2}$ states as intermediate states. We ignore the hyperfine splitting when computing the denominator in the expression

The incoming laser propagating along $\hat{y}$ has linear polarization $\hat{\epsilon}_L$ (chosen along $\hat{z}$ without loss of generality), the detection direction is defined by the angle θ relative to $\hat{\epsilon}_L$, and the polarization $\hat{\epsilon}_s$ of the scattered light is decomposed into components along $\hat{\epsilon}_1$ and $\hat{\epsilon}_2$ which are orthogonal to each other.

Following the formalism discussed in Refs. [32,34], the scattering rate for a transition from state $|i\rangle$ to state $|f\rangle$ via all intermediate states $|e\rangle$, with emitted light of polarization $\hat{\epsilon}_s$ is given by

$$R(i, f, \hat{\epsilon}_s, \hat{\epsilon}_L) \propto \int \left|\sum_e \frac{Q(\hat{\epsilon}_L, i, e)\langle e|\boldsymbol{d}.\hat{\epsilon}_s|f\rangle}{\left(\omega_{ef} - \omega_s - \frac{i\Gamma}{2}\right)}\tilde{G}(\omega)\right|^2 d\omega_s. \tag{B1}$$

Here, $\hat{\epsilon}_L$ is the polarization of the excitation laser and we choose this to be $(0, 1, 0)$ in the spherical basis (e_-, e_0, e_+); $Q(\hat{\epsilon}_L, i, e)$ is the two-photon matrix element between $|i\rangle$ and $|e\rangle$; $\boldsymbol{d}$ is the dipole operator; ω_s is the frequency of the emitted photon, and $\hat{\epsilon}_s$ is either $\hat{\epsilon}_2$ [$= \cos\theta\,\hat{x} - \sin\theta\,\hat{z}$ in the Cartesian coordinate system which is $(\frac{\cos\theta}{\sqrt{2}}, -\sin\theta, \frac{-\cos\theta}{\sqrt{2}})$ in the spherical basis] or $\hat{\epsilon}_1$ [$= \hat{y}$ in the Cartesian coordinate system which is $(\frac{i}{\sqrt{2}}, 0, \frac{i}{\sqrt{2}})$ in the spherical basis]. In the spherical basis the dot product $\hat{\epsilon}_s.\boldsymbol{d} = \sum_q (-1)^q \epsilon_{-q} d_q$ and we have to compute the sum separately for the two possible scattered polarizations. $\tilde{G}(\omega)$ accounts for broadening mechanisms.

The vectors of matrix elements $\langle e|\boldsymbol{d}|f\rangle$ are given by

for $Q(\hat{\epsilon}_L, i, e)$, but the fine structure is significant and is included in the calculations. The single photon detuning of the laser from the intermediate $6p_{1/2}$ state [$\Delta_{1/2} = \omega_L - \omega(p_{1/2})$] is approximately 55.3 THz, whereas that from the $6p_{3/2}$ state [$\Delta_{3/2} = \omega_L - \omega(p_{3/2})$] is approximately 38.7 THz. Thus we use $\Delta_{3/2} = 0.7\,\Delta_{1/2}$ in the calculations.

The laser transit time broadening is included by considering that the atom passing through the laser beam experiences an intensity pulse $I_0 e^{-\gamma^2 t^2}$, the Fourier transform of which is defined following Ref. [34]:

$$\tilde{G}(\omega) = 2\int E_+(t)\,E_-(t)\,e^{2i\omega t}\,dt \propto 2\,(\sqrt{\pi}/\gamma)\,e^{-(\omega-\omega_L)^2/\gamma^2}, \tag{B4}$$

where $E_+(t)$ and $E_-(t)$ represent the electric fields of the two counterpropagating light waves, and ω_L is the (monochromatic) laser frequency.

Substituting $\omega_s = 2\omega - \omega_{fi}$ and $\omega_{ef} + \omega_{fi} = \omega_{ei}$ into the expression for $R(i, f, \hat{\epsilon}_s, \hat{\epsilon}_L)$, we have

$$R(i, f, \hat{\epsilon}_s, \hat{\epsilon}_L) \propto \int_{-\infty}^{\infty} \left| \sum_e \frac{Q(\hat{\epsilon}_L, i, e)\langle e|\boldsymbol{d}.\hat{\epsilon}_s|f\rangle}{(\omega_{ei} - 2\omega - i\Gamma/2)} e^{-(\omega-\omega_L)^2/\gamma^2} \right|^2 d\omega$$

$$= \sum_{e,e'} Q(\hat{\epsilon}_L, i, e)\, e|\boldsymbol{d}.\hat{\epsilon}_s|f \{Q(\hat{\epsilon}_L, i, e')e'|\boldsymbol{d}.\hat{\epsilon}_s|f\}^* \frac{\pi \left(e^{(\Gamma - 2i\Delta_e)^2/8\gamma^2}\text{Erfc}\left[\frac{\Gamma - 2i\Delta_e}{2\sqrt{2}\gamma}\right] + e^{(\Gamma + 2i\Delta_{e'})^2/8\gamma^2}\text{Erfc}\left[\frac{\Gamma + 2i\Delta_{e'}}{2\sqrt{2}\gamma}\right] \right)}{\Gamma - i(\Delta_e - \Delta_{e'})}$$

$$= \sum_{e,e'} Q(\hat{\epsilon}_L, i, e)\langle e|\boldsymbol{d}.\hat{\epsilon}_s|f\rangle \{Q(\hat{\epsilon}_L, i, e')\langle e|\boldsymbol{d}.\hat{\epsilon}_s|f\rangle\langle e'|\boldsymbol{d}.\hat{\epsilon}_s f|\rangle\}^* \frac{\pi \left(f\left[\frac{-1}{i}\frac{\Gamma - 2i\Delta_e}{2\sqrt{2}\gamma}\right] + f\left[\frac{-1}{i}\frac{\Gamma + 2i\Delta_{e'}}{2\sqrt{2}\,\gamma}\right] \right)}{\Gamma - i(\Delta_e - \Delta_{e'})} .. \tag{B5}$$

Here $\Delta_e = \omega_{ei} - 2\omega_L$ and $f[z] = e^{-z^2}\text{Erfc}[-i\,z]$ is the Faddeeva W function.

To simulate the spectrum, we calculate the sum assuming equal initial population in all the Zeeman sublevels of the Cs hyperfine ground states $F = 3$ and $F = 4$. For the $7d_{5/2}$ state spectra, we consider the detected decay to the $6p_{3/2}$ state which comprises the $F'' = 2,3,4,5$ hyperfine levels. For the $7d_{3/2}$ state spectra, we consider the detected decay to the $6p_{1/2}$ state which comprises the $F'' = 3,4$ hyperfine levels. This gives an expression for the scattering detected in an infinitesimal solid angle around the detector direction θ. We then need to correct for the solid angle $\Omega_c = 2\pi(1 - \cos\theta_c)$ of the circular collection lens which has half angle θ_c. We express all the angular dependence in terms of the second Legendre polynomial, $P_2(\cos\theta)$, and then correct for the solid angle of the lens by making the replacement $P_2(\cos\theta) \rightarrow g(\theta_c)\, P_2(\cos\theta)$, where $g(\theta_c) = \cos\theta_c \cos^2(\theta_c/2)$ as derived in Ref. [32].

[1] M. I. Eides, H. Grotch, and V. A. Shelyuto, Theory of light hydrogenlike atoms, Phys. Rep. **342**, 63 (2001).

[2] S. G. Karshenboim, Precision physics of simple atoms: QED Tests, nuclear structure and fundamental constants, Phys. Rep. **422**, 1 (2005).

[3] A. Beyer, L. Maisenbacher, A. Matveev, R. Pohl, K. Khabarova, A. Grinin, T. Lamour, D. C. Yost, T. W. Hänsch, N. Kolachevsky, and T. Udem, The rydberg constant and proton size from atomic hydrogen, Science **358**, 79 (2017).

[4] A. Grinin, A. Matveev, D. C. Yost, L. Maisenbacher, V. Wirthl, R. Pohl, T. W. Hänsch, and T. Udem, Two-photon frequency comb spectroscopy atomic hydrogen, Science **370**, 1061 (2020).

[5] R. Lange, N. Huntemann, J. M. Rahm, C. Sanner, H. Shao, B. Lipphardt, C. Tamm, S. Weyers, and E. Peik, Improved limits for violations of local position invariance from atomic clock comparisons, Phys. Rev. Lett. **126**, 011102 (2021).

[6] C. J. Kennedy, E. Oelker, J. M. Robinson, T. Bothwell, D. Kedar, W. R. Milner, G. E. Marti, A. Derevianko, and J. Ye, Precision metrology meets cosmology: improved constraints on ultralight dark matter from atom-cavity frequency comparisons, Phys. Rev. Lett. **125**, 201302 (2020).

[7] C. Solaro, S. Meyer, K. Fisher, J. C. Berengut, E. Fuchs, and M. Drewsen, Improved isotope-shift-based bounds on bosons beyond the standard model through measurements of the ^{2}D$_{3/2}$-^{2}D$_{5/2}$ Interval in Ca$^+$, Phys. Rev. Lett. **125**, 123003 (2020).

[8] I. Counts, J. Hur, D. P. L. A. Craik, H. Jeon, C. Leung, J. C. Berengut, A. Geddes, A. Kawasaki, W. Jhe, and V. Vuletic, Evidence for nonlinear isotope shift in Yb$^+$ Search for new boson, Phys. Rev. Lett. **125**, 123002 (2020).

[9] N. L. Figueroa, J. C. Berengut, V. A. Dzuba, V. V. Flambaum, D. Budker, and D. Antypas, Precision determination of isotope shifts in ytterbium and implications for new physics, Phys. Rev. Lett. **128**, 073001 (2022).

[10] A. D. Ludlow, M. M. Boyd, J. Ye, E. Peik, and P. O. Schmidt, Optical atomic clocks, Rev. Mod. Phys. **87**, 637 (2015).

[11] F. Biraben, B. Cagnac, and G. Grynberg, Experimental evidence of two-photon transition without doppler broadening, Phys. Rev. Lett. **32**, 643 (1974).

[12] T. W. Hänsch, S. A. Lee, R. Wallenstein, and C. Wieman, Doppler-free two-photon spectroscopy of hydrogen 1S-2S*, Phys. Rev. Lett. **34**, 307 (1975).

[13] C. G. Parthey *et al.*, Improved measurement of the hydrogen 1S–2S transition frequency, Phys. Rev. Lett. **107**, 203001 (2011).

[14] H. Fleurbaey, S. Galtier, S. Thomas, M. Bonnaud, L. Julien, F. Biraben, F. Nez, M. Abgrall, and J. Guéna, New measurement of the 1S –3S transition frequency of hydrogen: contribution to the proton charge radius puzzle, Phys. Rev. Lett. **120**, 183001 (2018).

[15] M. Allegrini, E. Arimondo, and L. A. Orozco, Survey of hyperfine structure measurements in alkali atoms, J. Phys. Chem. Ref. Data **51**, 043102 (2022).

[16] B. Rahaman and S. Dutta, Hyperfine coupling constants of the cesium $7d_{5/2}$ state measured up to the octupole term, Opt. Lett. **47**, 4612 (2022).

[17] B. Rahaman and S. Dutta, High-Precision measurement of the hyperfine splitting and AC stark shift of the $7d$ $^2D_{3/2}$ State in atomic cesium, Phys. Rev. A **106**, 042811 (2022).

[18] V. A. Dzuba, V. V. Flambaum, and J. S. M. Ginges, Calculations of parity-nonconserving s–d amplitudes in Cs, Fr, Ba$^+$ and Ra$^+$, Phys. Rev. A **63**, 062101 (2001).

[19] B. M. Roberts, V. A. Dzuba, and V. V. Flambaum, Nuclear-Spin-Dependent parity nonconservation in s−d$_{5/2}$ and s − d$_{3/2}$ Transitions, Phys. Rev. A **89**, 012502 (2014).

[20] K. W. Martin, G. Phelps, N. D. Lemke, M. S. Bigelow, B. Stuhl, M. Wojcik, M. Holt, I. Coddington, M. W. Bishop, and J. H. Burke, Compact optical atomic clock based on a

two-photon transition in rubidium, Phys. Rev. Appl. **9**, 014019 (2018).

[21] Z. L. Newman, V. Maurice, C. Fredrick, T. Fortier, H. Leopardi, L. Hollberg, S. A. Diddams, J. Kitching, and M. T. Hummon, High-performance, compact optical standard, Opt. Lett. **46**, 4702 (2021).

[22] J. A. Quirk, A. Damitz, C. E. Tanner, and D. S. Elliott, Measurement of the hyperfine coupling constants and absolute energies of the $12s\,^2S_{1/2}$, $13s\,^2S_{1/2}$, and $11d\,^2D_J$ Levels in atomic cesium, Phys. Rev. A **105**, 022819 (2022).

[23] J. E. Stalnaker, V. Mbele, V. Gerginov, T. M. Fortier, S. A. Diddams, L. Hollberg, and C. E. Tanner, Femtosecond frequency comb measurement of absolute frequencies and hyperfine coupling constants in cesium vapor, Phys. Rev. A **81**, 043840 (2010).

[24] P. V. Kiran Kumar, M. Sankari, and M. V. Suryanarayana, Hyperfine structure of the $7d\,^2D_{3/2}$ Level in cesium measured by doppler-free two-photon spectroscopy, Phys. Rev. A **87**, 012503 (2013).

[25] A. Kortyna, V. Fiore, and J. Farrar, Measurement of the cesium $7d\,^2D_{3/2}$ Hyperfine coupling constants in a thermal beam using two-photon fluorescence spectroscopy, Phys. Rev. A **77**, 062505 (2008).

[26] Y.-C. Lee, Y.-H. Chang, Y.-Y. Chang, Y.-Y. Chen, C.-C. Tsai, and H.-C. Chui, Hyperfine coupling constants of cesium 7D states using two-photon spectroscopy, Appl. Phys. B **105**, 391 (2011).

[27] S.-D. Wang, J.-P. Yuan, L.-R. Wang, L.-T. Xiao, and S.-T. Jia, Investigation on the Cs $6S_{1/2}$ to 7D electric quadrupole transition via monochromatic two-photon process at 767 Nm, Front. Phys. **16**, 12502 (2021).

[28] F. D. Colegrove, P. A. Franken, R. R. Lewis, and R. H. Sands, Novel method of spectroscopy with applications to precision fine structure measurements, Phys. Rev. Lett. **3**, 420 (1959).

[29] P. A. Franken, Interference effects in the resonance fluorescence of "crossed" excited atomic states, Phys. Rev. **121**, 508 (1961).

[30] M. Horbatsch and E. A. Hessels, Shifts from a distant neighboring resonance, Phys. Rev. A **82**, 052519 (2010).

[31] T. Udem, L. Maisenbacher, A. Matveev, V. Andreev, A. Grinin, A. Beyer, N. Kolachevsky, R. Pohl, D. C. Yost, and T. W. Hänsch, Quantum interference line shifts of broad dipole-allowed transitions, Ann. Phys. **531**, 1900044 (2019).

[32] R. C. Brown, S. Wu, J. V. Porto, C. J. Sansonetti, C. E. Simien, S. M. Brewer, J. N. Tan, and J. D. Gillaspy, Quantum interference and light polarization effects in unresolvable atomic lines: application to a precise measurement of the ^{6,7}Li D_2 Lines, Phys. Rev. A **87**, 032504 (2013).

[33] S. Hofsäss, J. E. Padilla-Castillo, S. C. Wright, S. Kray, R. Thomas, B. G. Sartakov, B. Ohayon, G. Meijer, and S. Truppe, High-resolution isotope-shift spectroscopy of Cd I, Phys. Rev. Res. **5**, 013043 (2023).

[34] D. C. Yost, A. Matveev, E. Peters, A. Beyer, T. W. Hänsch, and T. Udem, Quantum interference in two-photon frequency-comb spectroscopy, Phys. Rev. A **90**, 012512 (2014).

[35] H. Fleurbaey, F. Biraben, L. Julien, J. P. Karr, and F. Nez, Cross-damping effects in 1S–3S spectroscopy of hydrogen and deuterium, Phys. Rev. A **95**, 052503 (2017).

[36] P. Barakhshan, A. Marrs, A. Bhosale, B. Arora, R. Eigenmann, and M. S. Safronova, *Portal for High-Precision Atomic Data and Computation (Version 2.0, February 2022)* (University of Delaware, Newark, 2022), https://www.udel.edu/atom/

[37] See Supplemental Material at http://link.aps.org/supplemental/10.1103/PhysRevA.109.042820 for additional details of the experiment, the estimation of systematic errors, the measured hyperfine splittings, the expressions to determine the hyperfine coupling constants and the calculation of ac Stark shift.

[38] Y.-B. Tang, B.-Q. Lou, and T.-Y. Shi, Ab initio studies of electron correlation effects in magnetic dipolar hyperfine interaction of Cs, J. Phys. B **52**, 055002 (2019).

[39] M. Auzinsh, K. Bluss, R. Ferber, F. Gahbauer, A. Jarmola, M. S. Safronova, U. I. Safronova, and M. Tamanis, Level-Crossing spectroscopy of the 7, 9, and 10 $D_{5/2}$ States of ^{133}Cs and validation of relativistic many-body calculations of the polarizabilities and hyperfine constants, Phys. Rev. A **75**, 022502 (2007).

[40] F.-C. Li and Y.-B. Tang, Relativistic coupled-cluster analysis of the second-order effects on the hyperfine structure in ^{133}Cs, Phys. Rev. A **107**, 052807 (2023).

[41] B. K. Sahoo (private communication).